Transition metal dichalcogenide monolayers in an ultrashort optical pulse: Femtosecond currents and anisotropic electron dynamics

S. Azar Oliaei Motlagh, Vadym Apalkov, and Mark I. Stockman

Phys. Rev. B **103**, 155416 — Published 16 April 2021

DOI: 10.1103/PhysRevB.103.155416

Transition metal dichalcogenide monolayers in ultrashort optical pulse: femtosecond currents and anisotropic electron dynamics

S. Azar Oliaei Motlagh, Vadym Apalkov, and Mark I. Stockman
Center for Nano-Optics (CeNO) and Department of Physics and Astronomy, Georgia State University, Atlanta, Georgia 30303, USA
(Dated: March 22, 2021)

We theoretically study the interaction of an ultrafast intense linearly polarized optical pulse with monolayers of transition metal dichalcogenides (TMDCs). Such a strong pulse redistributes electrons between the bands and generates femtosecond currents during the pulse. Due to the large bandwidth of the incident pulse, this process is completely an off-resonant. While in TMDCs, the time-reversal symmetry is conserved, the inversion symmetry is broken, and these monolayers have axial symmetry along the armchair direction but not along with the zigzag one. The pulse, polarized along with asymmetric directions of TMDC monolayer, generates both longitudinal, i.e., along the direction of polarization, and transverse, i.e., in the perpendicular direction, currents. Such currents result in charge transfer through the system. We study different TMDC materials and show how the femtosecond transport in TMDC monolayers depend on their parameters, such as lattice constant and bandgap.

I. INTRODUCTION

Nowadays, the femtosecond and strong fields driven phenomena, such as high harmonic generations, ultrafast ionization and metalization, nonlinear current generations, and nonlinear optical absorption in solids, attract growing interest due to their possible applications in ultrafast optical switches, optoelectronic devices, and ultimately in ultrafast information processing[1–28]. Among solids, transition metal dichalcogenides (TMDCs) have a special place due to their unique optical and transport properties. The bulk TMDCs are the stacks of monolayers, which are bounded by the van der Waals forces[29,30]. Due to the natural weakness of these forces, the bulk can be easily exfoliated to atomically thin monolayers[30,31]. Each monolayer consists of a single layer of transition metal atoms such as Mo or W, which is sandwiched between two chalcogin (S, Se, Te) layers.

The TMDC monolayers are direct bandgap semiconductors with the bandgaps of 1.1-2.5 eV[32–34]. Similar to graphene, TMDC monolayers have a honeycomb crystal structure, but they are not centrosymmetric, and their inversion symmetry is broken. Due to broken inversion symmetry, the Berry curvature is not singular as in graphene but has finite values with the opposite signs at two valleys, K, and K'. The finite Berry curvature results in an anomalous Hall effect in the absence of an external magnetic field[35] Another difference between TMDC materials and graphene is a strong intrinsic spin orbit coupling[36] in TMDCs, which results in relatively large spin splitting of the valence band (VB) and the conduction band (CB)[36] that makes TMDC monolayers suitable for spintronic applications.

Previously, we have shown that a single cycle of a circularly polarized optical pulse induces a large valley polarization, $\eta_v \geq 40\% - 60\%$, in TMDC monolayers, MoS_2 and WS_2[19]. Such fundamentally fastest valley polarization in TMDC monolayers is independent of electron spin and has a topological origin. Predominant population of one of the valleys in TMDC monolayer is not due to optical selection rules as in the case of a continuous wave but due to the topological resonance, which is a competition of the dynamic phase and the topological phase that is accumulated during an ultrashort and strong pulse[19]. It has also been recently predicted that the valley polarization could be tuned by the bandgap in gapped graphene monolayers[37]. In gapped graphene, the inversion symmetry is broken by placing graphene on a substrate, e.g., SiC, which reduces the point group symmetry of graphene from D_{6h} to D_{3h}[38,39], which is also the group symmetry of TMDC monolayers.

In the field of the intense optical pulse, the valence and the conduction band states are strongly coupled, which results in the generation of nonlinear electric currents and the transfer of electric charge through the system. Thus the ultrafast optical pulses can control the transport properties of electron systems and enhance their conductivity on the femtosecond time scale. Understanding the extent of such control is important for possible device application of solids. In the present paper, we study the femtosecond currents driven by intensive ultrashort laser pulses in different TMDC monolayers. We show how the characteristic parameters of TMDC materials, such as energy dispersion and the lattice constant, affect the generated electric current and corresponding transferred charge. The response of TMDC monolayer to the optical pulse is also anisotropic and depends on its polarization[40].

II. MAIN EQUATIONS

We assume that the free carrier relaxation, electron-hole recombination and carrier-phonon and electron-electron scattering times in TMDC monolayers[41–46] are longer than the characteristic duration of the optical pulse, ≈ 10 fs. In this case the electron dynamics due to the field of the pulse is coherent and is described by the

	MoS_2	WS_2	$MoSe_2$	WSe_2	$MoTe_2$	WTe_2
a (Å)	3.19	3.191	3.326	3.325	3.557	3.560
λ (eV)	0.073	0.211	0.091	0.228	0.107	0.237
$\Delta_K^{\rm Up} = \Delta_{K'}^{\rm Down}$ (eV)	1.590	1.600	1.346	1.325	0.967	0.835
$\Delta_K^{\rm Down} = \Delta_{K'}^{\rm Up}$ (eV)	1.736	2.023	1.526	1.776	1.180	1.307

TABLE I. Lattice constant, spin orbit coupling constant, and bandgap (for spin up and spin down) at the K and K' points for different TMDC monolayers[36].

Schrodinger equation with the time-dependent Hamiltonian, which has the following form

$$H(t) = H_0 - e\mathbf{r}\cdot\mathbf{F}(t), \tag{1}$$

where H_0 is the field-free Hamiltonian of monolayer TMDC, e is an electron charge, $\mathbf{r}$ is a position vector, and $\mathbf{F}(t)$ is the electric field of the pulse.

The crystal structure of the TMDC monolayer is shown in Fig. 1. It has D_{3h} symmetry and consists of two sublattices A and B, which are occupied by transition metal atoms (sublattice A) and chalcogen atoms (sublattice B). The first Brillouin zone of TMDC monolayer is a hexagon with two valleys, K and K' - see Fig. 1(c). We describe TMDC monolayer within a three band tight binding model[36]. In this model only the couplings between the nearest neighbor d orbitals (d_{xy}, d_{z^2}, and $d_{x^2-y^2}$) of transition metal atoms are considered. The corresponding Hamiltonian H_0 is the sum of the nearest neighbor tight-binding Hamiltonian $H^{(\rm TNN)}$, and spin orbit coupling (SOC) Hamiltonian $H^{(\rm SOC)}$[36],

$$\begin{aligned} H_0(\mathbf{k}) &= I\otimes H^{(\rm TNN)} + H^{(\rm SOC)} \\ &= \begin{bmatrix} H^{(\rm TNN)}(\mathbf{k}) + \frac{\lambda}{2}L_z & 0 \\ 0 & H^{(\rm TNN)}(\mathbf{k}) - \frac{\lambda}{2}L_z \end{bmatrix} \\ &= \begin{bmatrix} H^{\uparrow}_{3\times3}(\mathbf{k}) & 0 \\ 0 & H^{\downarrow}_{3\times3}(\mathbf{k}) \end{bmatrix}, \end{aligned} \tag{2}$$

where $\uparrow$ and $\downarrow$ correspond to spin up and spin down components, respectively, (3×3) tight binding matrix $H^{(\rm TNN)}$ is given in Appendix A, λ is the SOC constant[36], and

$$L_z = \begin{bmatrix} 0 & 0 & 0 \\ 0 & 0 & 2i \\ 0 & -2i & 0 \end{bmatrix}. \tag{3}$$

For each spin component, the tight binding model's band structure consists of three bands: one valence band (VB) and two conduction bands (CBs). Note that an external electric field does not couple the two spin components, so we can study the electron dynamics due to the field of the pulse for each spin component independently.

The main parameters of TMDC monolayers, which are the bandgap, lattice constant, and SOC constant, are shown in Table I. The lattice constant is in the range of $3.19 - 3.56$ Å, while the bandgap is between 0.8 eV and 2.0 eV.

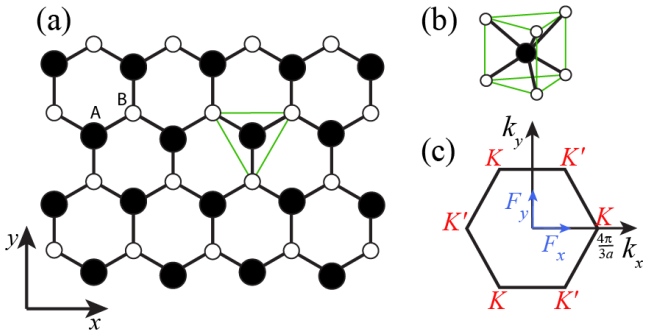

FIG. 1. (Color online) Crystal structure of TMDC monolayer. (a,b) Honeycomb crystal structure of TMDC monolayer consists of two sublattices: A and B. Sublattice A is occupied by transition metal atoms (closed dots), while sublatice B is occupied by chalcogen atoms (open dots). (c) The first Brillouin zone with two valleys, K and K'. For general polarization of the optical pulse, the electric field in the pulse has both x and y components, F_x and F_y.

For the pulse, which is linearly polarized in the x-direction, the electric field is given by the following expression

$$F_x(t) = F_0(1-2u^2)e^{-u^2}, \quad F_y(t) = 0, \tag{4}$$

where $u = t/\tau$, $\tau = 1$ fs is the pulse duration, and F_0 is the amplitude of the pulse.

The coherent electron dynamics is determined by a solution of the corresponding time dependent Schrodinger equation (TDSE)

$$i\hbar\frac{d\Psi(t)}{dt} = H(t)\Psi(t). \tag{5}$$

It is convenient to express this solution in the basis of time dependent Houston functions[47]

$$\Phi^{(H)}_{\alpha\mathbf{q}}(\mathbf{r},t) = \Psi^{(\alpha)}_{\mathbf{k}(\mathbf{q},t)}(\mathbf{r})\exp\left(i\phi^{(D)}_\alpha(q,t) + i\phi^{(B)}_\alpha(q,t)\right), \tag{6}$$

where $\Psi^{(\alpha)}_{\mathbf{k}}(\mathbf{r})$ are the eigenfunctions of field-free Hamiltonian H_0, $\phi^{(D)}_\alpha(q,t) = -\frac{1}{\hbar}\int dt' E_\alpha[\mathbf{k}(\mathbf{q},t')]$ is the dynamic phase, E_α are the eigenvalues of H_0, $\phi^{(B)}_\alpha(q,t) = -\frac{e}{\hbar}\int dt'\mathbf{F}(t')\mathbf{A}_{\alpha\alpha}[\mathbf{k}(\mathbf{q},t')]$ is the Berry phase, $\mathbf{A}_{\alpha\alpha}$ is the Berry connection, which is defined below by Eq. (16), and $\alpha\in\{v,c_1,c_2\}$ where v,c_1,c_2 denote the VB and two CBs, respectively. The electron trajectory in the reciprocal space, $\mathbf{k}(\mathbf{q},t)$, is determined by the Bloch acceleration theorem[48],

$$\mathbf{k}(\mathbf{q},t) = \mathbf{q} + \frac{e}{\hbar}\int_{-\infty}^{t}\mathbf{F}(t')dt', \tag{7}$$

where $\mathbf{q}$ is the initial crystal wave vector.

In the basis of Houston functions, solutions of the time dependent Schrodinger equation (5) are parameterized by

initial crystal wave vector $\mathbf{q}$ and are given by the following expression

$$\Psi_{\mathbf{q}}(\mathbf{r},t) = \sum_{\alpha=c_1,c_2,v} \beta_{\alpha\mathbf{q}}(t)\Phi^{(\mathrm{H})}_{\alpha\mathbf{q}}(\mathbf{r},t), \tag{8}$$

where $\beta_{\alpha\mathbf{q}}(t)$ are expansion coefficients, which satisfy the following system of differential equations

$$i\hbar\frac{\partial B_{\mathbf{q}}(t)}{\partial t} = H'(\mathbf{q},t)B_{\mathbf{q}}(t)\ . \tag{9}$$

The above system of equations is written using the following matrix notations

$$B_{\mathbf{q}}(t) = \begin{bmatrix}\beta_{c_2\mathbf{q}}(t)\\ \beta_{c_1\mathbf{q}}(t)\\ \beta_{v\mathbf{q}}(t)\end{bmatrix}\ , \tag{10}$$

$$H'(\mathbf{q},t) = -e\mathbf{F}(t)\cdot\hat{\boldsymbol{\mathcal{A}}}(\mathbf{q},t)\ , \tag{11}$$

$$\hat{\boldsymbol{\mathcal{A}}}(\mathbf{q},t) = \begin{bmatrix}0 & \boldsymbol{\mathcal{D}}_{\mathrm{c_2c_1}}(\mathbf{q},t) & \boldsymbol{\mathcal{D}}_{\mathrm{c_2v}}(\mathbf{q},t)\\ \boldsymbol{\mathcal{D}}^*_{\mathrm{c_2c_1}}(\mathbf{q},t) & 0 & \boldsymbol{\mathcal{D}}_{\mathrm{c_1v}}(\mathbf{q},t)\\ \boldsymbol{\mathcal{D}}^*_{\mathrm{c_2v}}(\mathbf{q},t) & \boldsymbol{\mathcal{D}}^*_{\mathrm{c_1v}}(\mathbf{q},t) & 0\end{bmatrix}. \tag{12}$$

where

$$\boldsymbol{\mathcal{D}}_{\alpha\alpha_1}(\mathbf{q},t) = \boldsymbol{\mathcal{A}}_{\alpha\alpha_1}[\mathbf{k}(\mathbf{q},t)]\times \exp\left(i\phi^{(\mathrm{D})}_{\alpha\alpha_1}(\mathbf{q},t) + i\phi^{(\mathrm{B})}_{\alpha\alpha_1}(\mathbf{q},)t\right), \tag{13}$$

$$\phi^{(\mathrm{D})}_{\alpha\alpha_1}(\mathbf{q},t) = \phi^{(\mathrm{D})}_{\alpha_1}(\mathbf{q},t) - \phi^{(\mathrm{D})}_{\alpha}(\mathbf{q},t), \tag{14}$$

$$\phi^{(\mathrm{B})}_{\alpha\alpha_1}(\mathbf{q},t) = \phi^{(\mathrm{B})}_{\alpha_1}(\mathbf{q},t) - \phi^{(\mathrm{B})}_{\alpha}(\mathbf{q},t), \tag{15}$$

$$\boldsymbol{\mathcal{A}}_{\alpha\alpha_1}(\mathbf{q}) = \left\langle \Psi^{(\alpha)}_{\mathbf{q}}|i\frac{\partial}{\partial\mathbf{q}}|\Psi^{(\alpha_1)}_{\mathbf{q}}\right\rangle. \tag{16}$$

Here, $\boldsymbol{\mathcal{A}}_{\alpha\alpha_1}(\mathbf{k})$ is the non-Abelian Berry connection[49–51].

The femtosecond field-driven currents in solids generally have two main contributions, which come from the interband and intraband dynamics. While these contributions are not gauge invariant, the total current, which is their sum, is gauge invariant[52]. We use the following expressions to calculate the intraband, $\mathbf{J}_{\mathrm{ra}}$, and interband, $\mathbf{J}_{\mathrm{er}}$, currents,

$$\mathbf{J}_{\mathrm{ra}}(t) = \frac{e}{a^2}\sum_{g_s}\sum_{\alpha=\mathrm{v,c_1,c_2},\mathbf{q}} |\beta_{\alpha,g_s}(\mathbf{q},t)|^2\,\mathbf{v}_{\alpha,g_s}(\mathbf{k}(\mathbf{q},t))\ , \tag{17}$$

$$\mathbf{J}_{\mathrm{er}}(t) = i\frac{e}{\hbar a^2}\sum_{g_s}\sum_{\substack{\mathbf{q}\\ \alpha,\alpha'=\mathrm{v,c_1,c_2}\\ \alpha\neq\alpha'}} \beta^*_{\alpha',g_s}(\mathbf{q},t)\beta_{\alpha,g_s}(\mathbf{q},t) \times\exp\{i\phi^{(\mathrm{D})}_{\alpha'\alpha,\mathrm{g_s}}(\mathbf{q},t) + i\phi^{(\mathrm{B})}_{\alpha'\alpha,\mathrm{g_s}}(\mathbf{q},t)\} \times\left[E_{\alpha',g_s}(\mathbf{k}(\mathbf{q},t)) - E_{\alpha,g_s}(\mathbf{k}(\mathbf{q},t))\right]\boldsymbol{\mathcal{A}}_{\alpha'\alpha,g_s}(\mathbf{k}(\mathbf{q},t))\,, \tag{18}$$

where $\mathbf{v}_{\alpha,g_s}(\mathbf{k}) = \frac{\partial}{\partial\mathbf{k}}E_{\alpha,g_s}(\mathbf{k}) + \dot{\mathbf{k}}\times\boldsymbol{\Omega}_{\alpha,g_s}$, $\boldsymbol{\Omega}_{\alpha,g_s}$is the Berry curvature ($\boldsymbol{\Omega}_{\alpha} = \boldsymbol{\nabla}\times\boldsymbol{\mathcal{A}}_{\alpha\alpha}$) and $g_s =\uparrow$ or $\downarrow$ is the component of the electron spin.

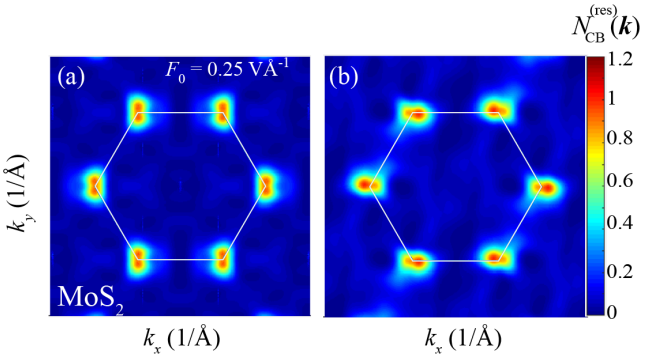

FIG. 2. (Color online) Residual CB population distribution in the reciprocal space. The distribution is shown for MoS_2 monolayer. The optical pulse is polarized in the (a) y direction and (b) x direction. The white solid lines show the boundary of the first Brillouin zone.

III. RESULTS AND DISCUSSION

A. CB population

Below we study the ultrafast electron dynamics in the following TMDC materials: MoS_2, WS_2, $MoSe_2$, WSe_2, $MoTe_2$, and WTe_2. Their tight-binding parameters are taken from Ref.[36] and are given in Appendix A. We apply a linearly polarized pulse propagating along z direction, i.e., perpendicular to the monolayer, with the amplitude of $\sim 0.1-0.5$ VÅ^{-1} and the duration of ~ 5 fs. Initially, i.e., before the pulse, the valence band is occupied, and the conduction bands are empty.

One the main characteristics of the electron dynamics due to the field of the pulse is CB population distribution in the reciprocal space, $N_{\mathrm{CB}}(\mathbf{k}) = |\beta_{\mathbf{C_1},\mathbf{k}}|^2 + |\beta_{\mathbf{C_2},\mathbf{k}}|^2$. Such distribution is nonzero during the pulse and its residual value, $N^{(\mathrm{res})}_{\mathrm{CB}}(\mathbf{k})$, determines the irreversibility of the electron dynamics. As theoretical and experimental studies have shown, the ultrafast electron dynamics is irreversible in 2D semimetals, e.g. graphene[13,53], 3D Weyl semimetals[54] and 2D semiconductors, e.g., black phosphorene[55] and TMDCs monolayers[19,56]. The residual CB population distribution, $N^{(\mathrm{res})}_{\mathrm{CB}}(\mathbf{k})$, also determines the valley polarization after a circularly polarized pulse[19].

For TMDC monolayers, the typical residual CB population distribution in the reciprocal space is shown in Fig. 2 for two polarizations of the pulse, along x and y directions. The amplitude of the pulse is 0.25 VÅ^{-1}. The CB population is large near the K and K' valleys, which is due to the large interband coupling at these two points. For such small field amplitude, 0.25 VÅ^{-1}, the electron excursion in the reciprocal space is relatively small, and the population distribution does not show any interference fringes, which are expected for large field amplitudes when the accumulation of the dynamic phase between

two passages of the K valleys is large enough to produce an interference pattern. The CB population is the same for both valleys. This is because the linearly polarized pulse preserves the time-reversal symmetry and does not induce any valley polarization. The residual valley polarization is expected only for a circularly polarized pulse, which breaks the time-reversal symmetry.

The CB population distribution for the pulse polarized in the y direction is shown in Fig. 2(a). Since the axis y is the axis of symmetry of the TMDC monolayer, the CB population distribution is symmetric with respect to the y axis both during the pulse and after the pulse. Because of such symmetry, the electric current is generated only in y direction during the pulse, while there is no current in the x direction.

A more interesting situation occurs for the pulse polarized in the x direction. In this case, the direction of polarization, i.e., the x direction, is not the axis of symmetry of TMDC monolayer, and the residual CB population distribution, which is shown in Fig. 2(b), clearly illustrates such asymmetry. Because the CB population distribution is not symmetric with respect to the x axis, the electric current is generated in both x and y directions. To study the effect of such asymmetry on the electron transport, below, we consider TMDC monolayers' response only to the pulse polarized in the x direction.

The current, generated during the pulse, is determined by the CB population distribution in the reciprocal space. In Fig. 3, we show the residual CB population, $N_{\rm CB}^{\rm (res)}(\mathbf{k})$, for different TMDC monolayers. For all TMDC materials, except $MoTe_2$, $N_{\rm CB}^{\rm (res)}(\mathbf{k})$ have similar distributions. Namely, they are concentrated at the K and K' points along both the k_x and k_y directions. Then, as we discuss in the next section, the corresponding electric currents, both longitudinal and transverse, i.e., along the direction of polarization of the pulse and in perpendicular direction, have similar time dependencies for all TMDC materials except $MoTe_2$.

Monolayer $MoTe_2$ has completely different residual CB population distribution. While along the direction of the pulse polarization, i.e., the x direction, $N_{\rm CB}^{\rm (res)}(\mathbf{k})$ is concentrated near the K and K' points, in the perpendicular direction, i.e., in the y direction, $N_{\rm CB}^{\rm (res)}(\mathbf{k})$ is highly delocalized and there is a large CB population along the lines connecting the K and K' points - see Fig. 3(c). Thus, along the x direction, $N_{\rm CB}^{\rm (res)}(\mathbf{k})$ of $MoTe_2$ behaves similar to $N_{\rm CB}^{\rm (res)}(\mathbf{k})$ of other TMDC materials, while, along the y direction, $N_{\rm CB}^{\rm (res)}(\mathbf{k})$ of $MoTe_2$ monolayer is much more extended compared to other TMDC monolayers. Such difference in the CB population distributions of $MoTe_2$ and other TMDC materials results in different properties of the corresponding generated electric currents, as shown in the next section.

B. Electric currents

As we discussed in the previous section, for the pulse polarized in the x direction, i.e., along the zigzag direction, both the x and y components of the current, J_x and J_y, are generated[40]. The y component of the current is due to the TMDC monolayer's asymmetry with respect to the x axis. Since such asymmetry also results in a finite bandgap of the system, there is a correlation between the value of the TMDC monolayer's bandgap and the magnitude of J_y. Namely, the y component of the current disappears for the system with zero bandgap, e.g., for pristine graphene, for which the x axis is also the axis of symmetry.

The generated electric currents for different TMDC materials are shown in Fig. 4 for the field amplitude of 0.25 V/Å. During the pulse, i.e, -2 fs $< t <$ 2 fs, the x component of the current has the same profile for all TMDC materials. This is consistent with the structure of the residual CB population distribution shown in Fig. 3, where, for all TMDC monolayers, $N_{\rm CB}^{\rm (res)}(\mathbf{k})$ as a function of k_x is concentrated near the K points. Thus the corresponding transport along the x direction is similar for all TMDC monolayers.

After the pulse, i.e., $t >$ 2 fs, the x component of the current, J_x, has oscillatory behavior with the frequency of oscillations that depends on the bandgap of TMDC monolayer. Here the bandgap is in the range of $1.1 - 2.1$ eV (see Table I). Such oscillations in the residual current J_x occurs because the main contribution to J_x is the interband one, while the intraband contribution, which depends only on the CB population distribution, is small.

Since the current in the y direction is due to the system's asymmetry, its magnitude is almost three times smaller than the magnitude of the current in the x direction (see Fig. 4). Current J_y shows the oscillatory behavior as a function of time with well pronounced bandgap-dependent oscillations after the pulse, see Fig. 4(a). During the pulse (-2 fs $< t <$ 2 fs), current J_y has almost the same time dependence for all TMDC monolayers except one, $MoTe_2$, which shows completely different profile. Such distinct behavior of $MoTe_2$ is consistent with unique CB population distribution for this material as shown in Fig. 3(c). Namely, $N_{\rm CB}^{\rm (res)}(\mathbf{k})$ as a function of k_y is highly delocalized along the lines connecting K points for $MoTe_2$ monolayer, while for other TMDCs $N_{\rm CB}^{\rm (res)}(\mathbf{k})$ is concentrated near the K and K' points.

The dependence of the electric current on the field amplitude, F_0, is shown in Fig. 5 for MoS_2 monolayer. For other TMDC materials, the dependence of the current on F_0 has a similar tendency. As expected, the generated current monotonically increases with F_0 while keeping the same profile during the pulse and the same oscillatory behavior after the pulse. Here the frequency of oscillations, which is determined by the bandgap, does not depend on F_0.

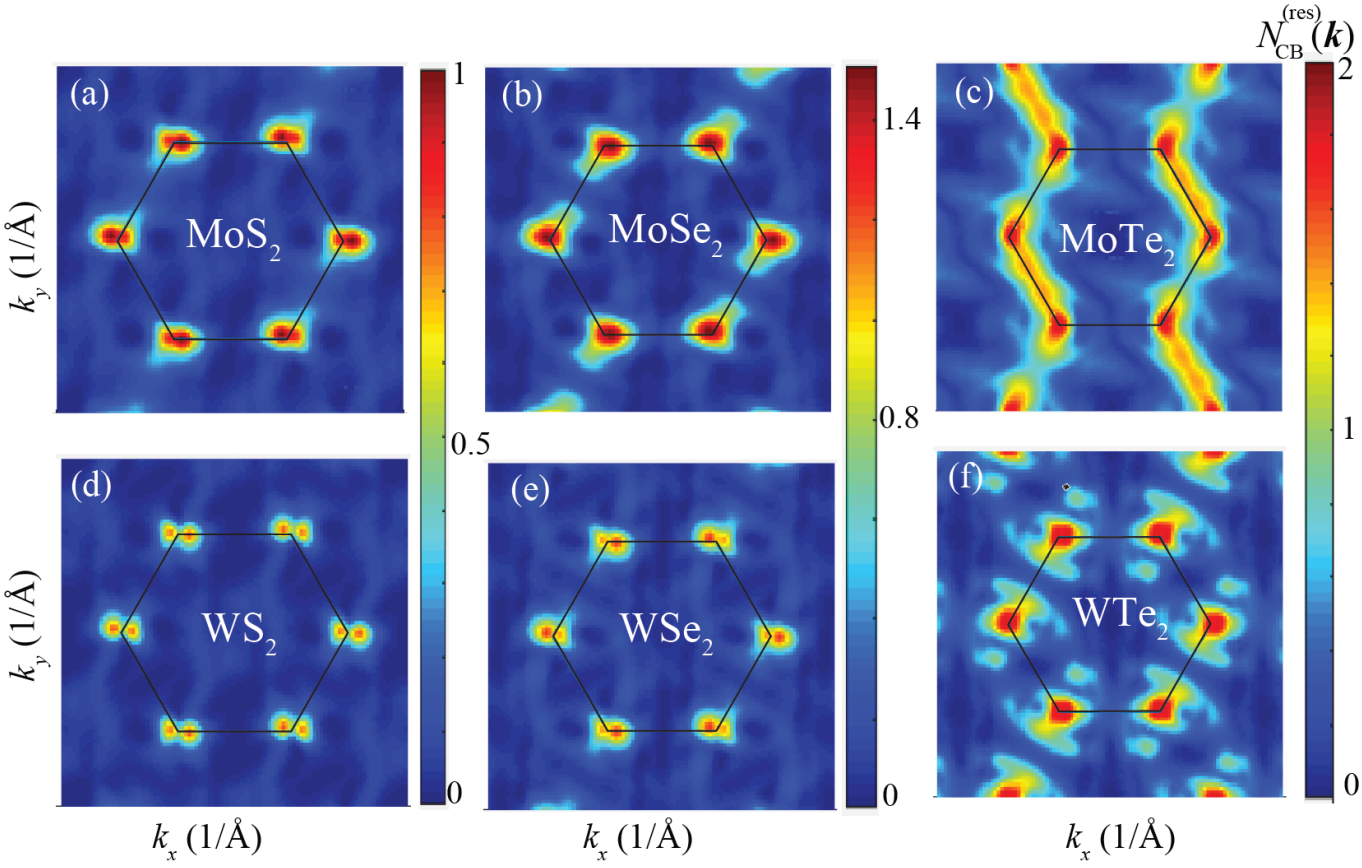

FIG. 3. (Color online) Residual CB population distributions in the reciprocal space for different TMDC monolayers: (a) MoS_2, (b) $MoSe_2$, (c) $MoTe_2$, (d) WS_2, (e) WSe_2, and (f) WTe_2. The optical pulse is linearly polarized in the x direction and its amplitude is 0.25 VÅ^{-1}. The solid black lines show the edges of the first Brillouin zone. For all TMDC monolayers, except $MoTe_2$, the CB population is concentrated near the K and K' points.

C. Transferred charge

One of the characteristics of nonlinearity of electron response to an ultrashort pulse is a charge transferred through the system during the pulse. Such a charge can also be measured experimentally[2,5]. It is defined by the following expression

$$\mathbf{Q} = \int_{-\infty}^{\infty} \mathbf{J}(t)\mathrm{d}t'. \tag{19}$$

Since the residual current shows an oscillating behavior, to eliminate the dependence on the upper limit in the above integral, we introduce a relaxation time of 5 fs and put the upper limit in the integral at 10 fs. The transferred charge is also the residual polarization of the system.

The transferred charge as a function of the field amplitude, F_0, is shown in Fig. 6 for different TMDC monolayers. The charge transferred along the y direction, Q_y, monotonically increases with F_0 - see Fig. 6(a). For all TMDC monolayers, except $MoTe_2$, the charge is transferred in the positive direction of the y axis, while for $MoTe_2$ the transfer of the charge occurs in the negative direction. Such directions of the transfer correspond to the condition that the pulse's field maximum is in the positive direction of the x axis. The magnitude of the transferred charge increases with decreasing the bandgap of the TMDC monolayer. The largest charge transfer occurs for WTe_2 monolayer, while the smallest - for $MoTe_2$ monolayer.

Along the x axis [see Fig. 6(b)], the charge is transferred in the direction of the field maximum for all TMDC monolayers. The dependence of Q_x on the pulse amplitude, F_0, is nonmonotonic. The transferred charge reaches its maximum at some value of $F_0 = F_{max}$ and then decreases with F_0. The value of F_{max} is partially correlated with the condition that at this field amplitude, an electron, which is initially at one of the valleys, say valley K, reaches another valley, K', during the pulse. For example, for TMDC monolayers with large lattice constants, $MoTe_2$: 3.557 Å and WTe_2 : 3.560 Å[36], the maxima occur at the lower field amplitudes. The lattice constant is not the only parameter that determines Q_x dependence on F_0. The transferred charge also depends

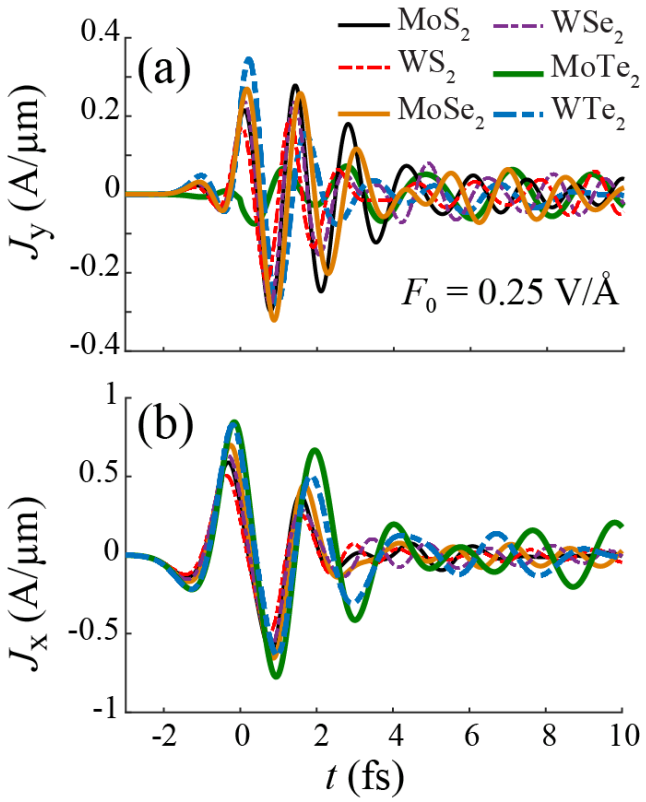

FIG. 4. (Color online) Femtosecond field driven currents as a function of time in different TMDC monolayers. The generated electric currents have both the y components (a) and the x components (b). The pulse is linearly polarized in the x direction and its amplitude is 0.25 VÅ^{-1}.

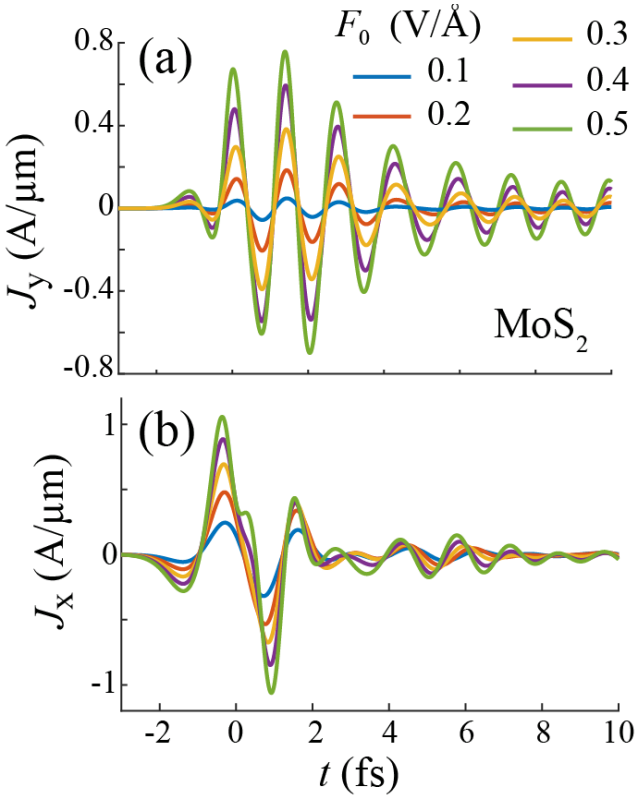

FIG. 5. (Color online) Ultrafast field driven currents in MoS_2 monolayer as a function of time for different field amplitudes. The y component (a) and the x component (b) of the current are shown. The optical pulse is linearly polarized in the x direction.

on the bandgap and spin-orbit coupling in the TMDC monolayer. In terms of applications, the data in Fig. 6(b) illustrate that $MoTe_2$ monolayer is the most sensitive to the pulse amplitude, i.e., for $MoTe_2$ monolayer, the transferred charge, Q_x, shows relatively sharp maximum with strong dependence on F_0.

IV. CONCLUSION

The TMDC monolayers have the symmetry group of D_{3h} and the broken inversion symmetry. With only three axes of symmetry, which are along with the armchair directions, the response of TMDC monolayer to an optical pulse is highly anisotropic. If the optical pulse is polarized along the direction of symmetry of the monolayer, then the electric current is generated only along the direction of polarization. But suppose the optical pulse's polarization is along a non-symmetric direction, for example, along the zigzag direction; in that case, the electric current has both longitudinal and transverse components, i.e., components along the direction of polarization and in the perpendicular direction. For all TMDC monolayers, the longitudinal electric current shows similar behavior as a function of time. The interband contribution mainly determines the generated electric current in TMDC monolayers. As a result, the residual current as a function of time shows oscillations, the frequency of which is determined by the bandgap of the corresponding TMDC monolayer. The generated electric current also transfers the electric charge through the system. For longitudinal currents, the charge is transferred in the direction of the field maximum of the pulse. As a function of the field amplitude, the transferred charge has a maximum, the position of which depends on the lattice constant of the TMDC monolayer. Among all TMDC materials, $MoTe_2$ monolayer is the most sensitive to the optical pulse parameters. The charge transferred through $MoTe_2$ monolayer shows strong depends on the field amplitude with a well-pronounced maximum at ≈ 0.3 V/Å.

The transverse current also results in the charge transfer through the system during the pulse. The magnitude of the transferred charge monotonically increases with the field amplitude, while the transfer's direction depends on the TMDC material. Control of electron transport on a femtosecond time scale paves the way for the ultrafast electronic application of TMDCs monolayers.

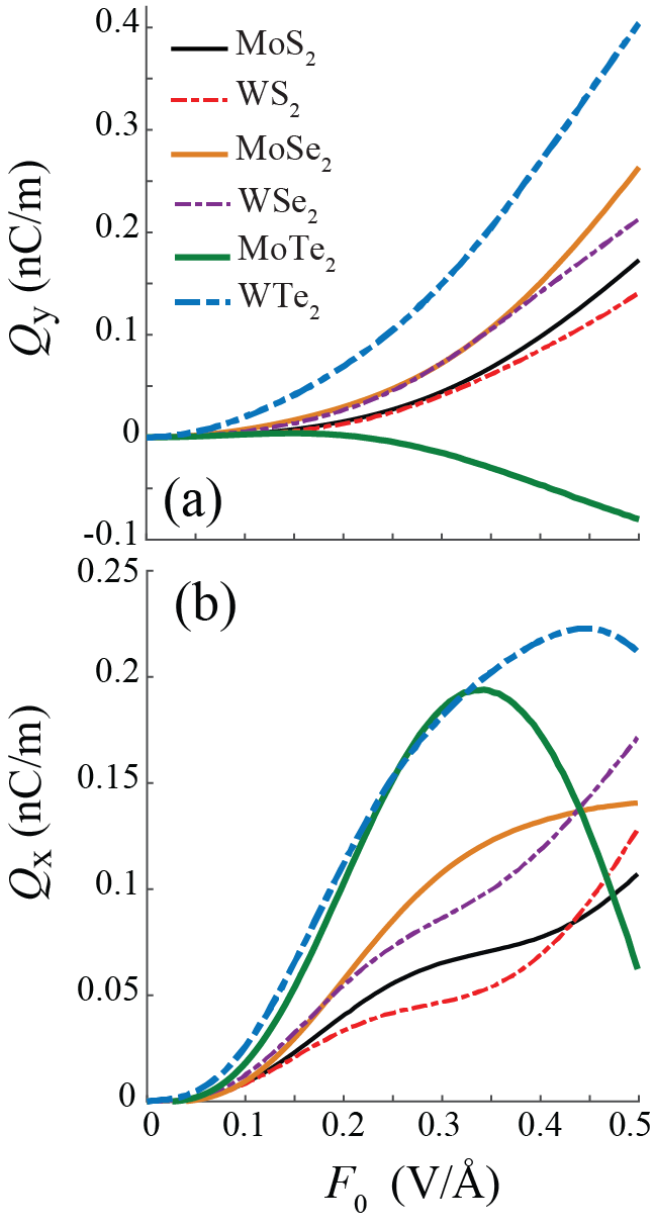

FIG. 6. (Color online) Charge transferred through the system during the pulse as a function of the field amplitude, F_0, for different TMDC monolayers. The transferred charge along the y direction (a) and the x direction (b) is shown. The optical pulse is linearly polarized in the x direction.

Appendix A: Tight binding Hamiltonian

The three band nearest-neighbor (TNN) tight-binding Hamiltonian, $H^{(\mathrm{TNN})}$, of TMDC monolayer takes into account three orbitals (d_{z^2}, d_{xy}, and $d_{x^2-y^2}$) of transition metal atoms[36]. The Hamiltonian is given by the following expression

$$H^{\mathrm{TNN}}(\mathbf{k}) = \begin{bmatrix} V_0 & V_1 & V_2 \\ V_1^* & V_{11} & V_{12} \\ V_2^* & V_{12}^* & V_{22} \end{bmatrix} , \qquad \text{(A1)}$$

where

$$
\begin{aligned}
V_0 &= \epsilon_1 + 2t_0(2\cos\alpha\cos\beta + \cos 2\alpha) + 2r_0(2\cos 3\alpha\cos\beta + \cos 2\beta) + 2u_0(2\cos 2\alpha\cos 2\beta + \cos 4\alpha)\ , \\
\mathrm{Re}[V_1] &= -2\sqrt{3}t_2\sin\alpha\sin\beta + 2(r_1 + r_2)\sin 3\alpha\sin\beta - 2\sqrt{3}u_2\sin 2\alpha\sin 2\beta\ , \\
\mathrm{Im}[V_1] &= 2t_1\sin\alpha(2\cos\alpha + \cos\beta) + 2(r_1 - r_2)\sin 3\alpha\cos\beta + 2u_1\sin 2\alpha(2\cos 2\alpha + \cos 2\beta)\ , \\
\mathrm{Re}[V_2] &= 2t_2(\cos 2\alpha - \cos\alpha\cos\beta) - \frac{2}{\sqrt{3}}(r_1 + r_2)(\cos 3\alpha\cos\beta - \cos 2\beta) + 2u_2(\cos 4\alpha - \cos 2\alpha\cos 2\beta)\ , \\
\mathrm{Im}[V_2] &= 2\sqrt{3}t_1\cos\alpha\sin\beta + \frac{2}{\sqrt{3}}\sin\beta(r_1 - r_2)(\cos 3\alpha + 2\cos\beta) + 2\sqrt{3}u_1\cos 2\alpha\sin 2\beta\ , \\
V_{11} &= \epsilon_2 + (t_{11} + 3t_{22})\cos\alpha\cos\beta + 2t_{11}\cos 2\alpha + 4r_{11}\cos 3\alpha\cos\beta + 2(r_{11} + \sqrt{3}r_{12}\cos 2\beta) + \\
&\quad (u_{11} + 3u_{22})\cos 2\alpha\cos 2\beta + 2u_{11}\cos 4\alpha\ , \\
\mathrm{Re}[V_{12}] &= \sqrt{3}(t_{22} - t_{11})\sin\alpha sin\beta + 4r_{12}\sin 3\alpha\sin\beta + \sqrt{3}(u_{22} - u_{11}\sin 2\alpha\sin 2\beta)\ , \\
\mathrm{Im}[V_{12}] &= 4t_{12}\sin\alpha(\cos\alpha - cos\beta) + 4u_{12}\sin 2\alpha(\cos 2\alpha - \cos 2\beta)\ , \\
V_{22} &= \epsilon_2 + (3t_{11} + t_{22})\cos\alpha\cos\beta + 2t_{22}\cos 2\alpha + 2r_{11}(2\cos 3\alpha\cos\beta + \cos 2\beta) + \\
&\quad \frac{2}{\sqrt{3}}r_{12}(4\cos 3\alpha\cos\beta - \cos 2\beta) + (3u_{11} + u_{22})\cos 2\alpha\cos 2\beta + 2u_{22}\cos 4\alpha\ ,
\end{aligned}
\tag{A2}
$$

and

$$
(\alpha, \beta) = \left(\frac{1}{2}k_x a, \frac{\sqrt{3}}{2}k_y a\right)\ . \tag{A3}
$$

The parameters in the above Hamiltonian are given in table II Ref [36] for different TMDC materials.

ACKNOWLEDGMENTS

Major funding was provided by Grant No. DE-FG02-01ER15213 from the Chemical Sciences, Biosciences, and Geosciences Division, Office of Basic Energy Sciences, Office of Science, US Department of Energy. Numerical simulations were performed using support by Grant No. DE-SC0007043 from the Materials Sciences and Engineering Division of the Office of the Basic Energy Sciences, Office of Science, US Department of Energy.

[1] Jonas Kiemle, Philipp Zimmermann, Alexander W. Holleitner, and Christoph Kastl, "Light-field and spin-orbit-driven currents in van der waals materials," Nanophotonics **9**, 2693 (2020).

[2] Shawn Sederberg, Dmitry Zimin, Sabine Keiber, Florian Siegrist, Michael S. Wismer, Vladislav S. Yakovlev, Isabella Floss, Christoph Lemell, Joachim Burgdrfer, Martin Schultze, Ferenc Krausz, and Nicholas Karpowicz, "Attosecond optoelectronic field measurement in solids," Nature Communications **11**, 430 (2020).

[3] A. Schiffrin, T. Paasch-Colberg, N. Karpowicz, V. Apalkov, D. Gerster, S. Muhlbrandt, M. Korbman, J. Reichert, M. Schultze, S. Holzner, J. V. Barth, R. Kienberger, R. Ernstorfer, V. S. Yakovlev, M. I. Stockman, and F. Krausz, "Optical-field-induced current in dielectrics," Nature **493**, 70–74 (2012).

[4] Jie Li, Jian Lu, Andrew Chew, Seunghwoi Han, Jialin Li, Yi Wu, He Wang, Shambhu Ghimire, and Zenghu Chang, "Attosecond science based on high harmonic generation from gases and solids," Nature Communications **11**, 2748 (2020).

[5] T. Paasch-Colberg, A. Schiffrin, N. Karpowicz, S. Kruchinin, Saglam Ozge, S. Keiber, O. Razskazovskaya, S. Muhlbrandt, A. Alnaser, M. Kubel, V. Apalkov, D. Gerster, J. Reichert, T. Wittmann, J. V. Barth, M. I. Stockman, R. Ernstorfer, V. S. Yakovlev, R. Kienberger, and F. Krausz, "Solid-state light-phase detector," Nat. Phot. **8**, 214–218 (2014).

[6] V. Apalkov and M. I. Stockman, "Theory of dielectric nanofilms in strong ultrafast optical fields," Phys. Rev. B **86**, 165118–1–13 (2012).

[7] Giulio Vampa, Jian Lu, Yong Sing You, Denitsa R Baykusheva, Mengxi Wu, Hanzhe Liu, Kenneth J Schafer, Mette B Gaarde, David A Reis, and Shambhu Ghimire, "Attosecond synchronization of extreme ultraviolet high harmonics from crystals," Journal of Physics B: Atomic, Molecular and Optical Physics **53**, 144003 (2020).

[8] T. Higuchi, C. Heide, K. Ullmann, H. B. Weber, and P. Hommelhoff, "Light-field-driven currents in graphene," Nature **550**, 224–228 (2017).

[9] Elisabeth Gruber, Richard A. Wilhelm, Rmi Ptuya, Valerie Smejkal, Roland Kozubek, Anke Hierzenberger, Bern-

	MoS_2	WS_2	$MoSe_2$	WSe_2	$MoTe_2$	WTe_2
a	3.19	3.191	3.326	3.325	3.557	3.560
ϵ_1	0.683	0.717	0.684	0.728	0.588	0.697
ϵ_2	1.707	1.916	1.546	1.655	1.303	1.380
t_0	-0.146	-0.152	-0.146	-0.146	-0.226	-0.109
t_1	-0.114	-0.097	-0.130	-0.124	-0.234	-0.164
t_2	0.506	0.590	0.432	0.507	0.036	0.368
t_{11}	0.085	0.047	0.144	0.117	0.400	0.204
t_{12}	0.162	0.178	0.117	0.127	0.098	0.093
t_{22}	0.073	0.016	0.075	0.015	0.017	0.038
r_0	0.06	0.069	0.039	0.036	0.003	-0.015
r_1	-0.236	-0.261	-0.209	-0.234	-0.025	-0.209
r_{11}	0.016	-0.003	0.052	0.044	0.082	0.115
r_{12}	0.087	0.109	0.060	0.075	0.051	0.009
r_2	0.067	0.107	0.069	0.107	-0.169	0.107
u_0	-0.038	-0.054	-0.042	-0.061	0.057	-0.066
u_1	0.046	0.045	0.036	0.032	0.103	0.011
u_2	0.001	0.002	0.008	0.007	0.187	-0.013
u_{11}	0.266	0.325	0.272	0.329	-0.045	0.312
u_{12}	-0.176	-0.206	-0.172	-0.202	-0.141	-0.177
u_{22}	-0.15	-0.163	-0.150	-0.164	0.087	-0.132
λ	0.073	0.211	0.091	0.228	0.107	0.237

TABLE II. Parameters of three band tight-binding Hamiltonian. Here the lattice constant, a, is in units of Å, while all other parameters are in units of eV[36].

hard C. Bayer, Iigo Aldazabal, Andrey K. Kazansky, Florian Libisch, Arkady V. Krasheninnikov, Marika Schleberger, Stefan Facsko, Andrei G. Borisov, Andrs Arnau, and Friedrich Aumayr, "Ultrafast electronic response of graphene to a strong and localized electric field," Nat. Commun. **7**, 13948 (2016).

[10] S. A. Oliaei Motlagh, V. Apalkov, and M. I. Stockman, "Interaction of crystalline topological insulator with an ultrashort laser pulse," Phys. Rev. B **95**, 085438–1–8 (2017).

[11] S. A. O. Motlagh, J. S. Wu, V. Apalkov, and M. I. Stockman, "Fundamentally fastest optical processes at the surface of a topological insulator," Phys. Rev. B **98**, 125410–1–11 (2018).

[12] C. Heide, T. Higuchi, H. B. Weber, and P. Hommelhoff, "Coherent electron trajectory control in graphene," Phys. Rev. Lett. **121**, 207401–1–5 (2018).

[13] Christian Heide, Tobias Boolakee, Takuya Higuchi, Heiko B Weber, and Peter Hommelhoff, "Interaction of carrier envelope phase-stable laser pulses with graphene: the transition from the weak-field to the strong-field regime," New J. Phys. **21**, 045003 (2019).

[14] Dong Sun, Grant Aivazian, Aaron M. Jones, Jason S. Ross, Wang Yao, David Cobden, and Xiaodong Xu, "Ultrafast hot-carrier-dominated photocurrent in graphene," Nat. Nanotechnol. **7**, 114 (2012).

[15] Hiroki Mashiko, Yuta Chisuga, Ikufumi Katayama, Katsuya Oguri, Hiroyuki Masuda, Jun Takeda, and Hideki Gotoh, "Multi-petahertz electron interference in cr:al2o3 solid-state material," Nat. Commun. **9**, 1468 (2018).

[16] Hee Jun Shin, Van Luan Nguyen, Seong Chu Lim, and Joo-Hiuk Son, "Ultrafast nonlinear travel of hot carriers driven by high-field terahertz pulse," J. Phys. B: At. Mol. Opt. Phys. **51**, 144003 (2018).

[17] Takuya Higuchi, Christian Heide, Konrad Ullmann, Heiko B. Weber, and Peter Hommelhoff, "Light-field-driven currents in graphene," Nature **550**, 224–228 (2017).

[18] M. Trushin, A. Grupp, G. Soavi, A. Budweg, D. De Fazio, U. Sassi, A. Lombardo, A. C. Ferrari, W. Belzig, A. Leitenstorfer, and D. Brida, "Ultrafast pseudospin dynamics in graphene," Phys. Rev. B **92**, 165429 (2015).

[19] S. A. Oliaei Motlagh, J.-S. Wu, V. Apalkov, and M. I. Stockman, "Femtosecond valley polarization and topological resonances in transition metal dichalcogenides," Phys. Rev. B **98**, 081406(R)–1–6 (2018).

[20] D. Sun, J. W. Lai, J. C. Ma, Q. S. Wang, and J. Liu, "Review of ultrafast spectroscopy studies of valley carrier dynamics in two-dimensional semiconducting transition metal dichalcogenides," Chin. Phys. B **26** (2017).

[21] Jun Zhang, Hao Ouyang, Xin Zheng, Jie You, Runze Chen, Tong Zhou, Yizhen Sui, Yu Liu, Xiang'ai Cheng, and Tian Jiang, "Ultrafast saturable absorption of mos2 nanosheets under different pulse-width excitation conditions," Opt. Lett. **43**, 243–246 (2018).

[22] Yong Sing You, Yanchun Yin, Yi Wu, Andrew Chew, Xiaoming Ren, Fengjiang Zhuang, Shima Gholam-Mirzaei, Michael Chini, Zenghu Chang, and Shambhu Ghimire, "High-harmonic generation in amorphous solids," Nat. Commun. **8**, 724 (2017).

[23] H. Z. Liu, Y. L. Li, Y. S. You, S. Ghimire, T. F. Heinz, and D. A. Reis, "High-harmonic generation from an atomically thin semiconductor," Nat. Phys. **13**, 262–266 (2017).

[24] A. Kaiser, B. Rethfeld, M. Vicanek, and G. Simon, "Microscopic processes in dielectrics under irradiation by subpicosecond laser pulses," Phys. Rev. B **61**, 11437–11450 (2000).

[25] H. G. Rosa, J. A. Castaneda, C. H. B. Cruz, L. A. Padilha, J. C. V. Gomes, E. A. T. de Souza, and H. L. Fragnito, "Controlled stacking of graphene monolayer saturable absorbers for ultrashort pulse generation in erbium-doped fiber lasers," Opt. Mater. Express **7**, 2528–2537 (2017).

[26] S. Kumar, M. Anija, N. Kamaraju, K. S. Vasu, K. S. Subrahmanyam, A. K. Sood, and C. N. R. Rao, "Femtosecond carrier dynamics and saturable absorption in graphene suspensions," Appl. Phys. Lett. **95** (2009).

[27] F. Gesuele, "Ultrafast hyperspectral transient absorption spectroscopy: Application to single layer graphene," Photonics **6** (2019).

[28] S. Azar Oliaei Motlagh, Ahmal Jawad Zafar, Aranyo Mitra, Vadym Apalkov, and Mark I. Stockman, "Ultrafast strong-field absorption in gapped graphene," Phys. Rev. B **101**, 165433 (2020).

[29] Q. H. Wang, K. Kalantar-Zadeh, A. Kis, J. N. Coleman, and M. S. Strano, "Electronics and optoelectronics of two-dimensional transition metal dichalcogenides," Nature Nanotechnology **7**, 699–712 (2012).

[30] K. S. Novoselov, A. Mishchenko, A. Carvalho, and A. H. C. Neto, "2d materials and van der Waals heterostructures," Science **353**, 461–1–11 (2016).

[31] D. Xiao, G. B. Liu, W. X. Feng, X. D. Xu, and W. Yao, "Coupled spin and valley physics in monolayers of MoS_2 and other group-VI dichalcogenides," Phys. Rev. Lett. **108** (2012).

[32] Kin Fai Mak, Changgu Lee, James Hone, Jie Shan, and Tony F. Heinz, "Atomically thin mos_2: A new direct-gap semiconductor," Phys. Rev. Lett. **105**, 136805 (2010).

[33] Hiram J. Conley, Bin Wang, Jed I. Ziegler, Richard F. Haglund, Sokrates T. Pantelides, and Kirill I. Bolotin, "Bandgap engineering of strained monolayer and bilayer

mos_2," **13**, 3626–3630 (2013), pMID: 23819588.

[34] Miguel M. Ugeda, Aaron J. Bradley, Su-Fei Shi, Felipe H. da Jornada, Yi Zhang, Diana Y. Qiu, Wei Ruan, Sung-Kwan Mo, Zahid Hussain, Zhi-Xun Shen, Feng Wang, Steven G. Louie, and Michael F. Crommie, "Giant bandgap renormalization and excitonic effects in a monolayer transition metal dichalcogenide semiconductor," Nature Materials **13**, 1091–1095 (2014).

[35] Naoto Nagaosa, Jairo Sinova, Shigeki Onoda, A. H. MacDonald, and N. P. Ong, "Anomalous Hall effect," Reviews of Modern Physics **82**, 1539–1592 (2010).

[36] G. B. Liu, W. Y. Shan, Y. G. Yao, W. Yao, and D. Xiao, "Three-band tight-binding model for monolayers of group-VIB transition metal dichalcogenides," Phys. Rev. B **88**, 085433–1–10 (2013).

[37] S. A. Oliaei Motlagh, F. Nematollahi, V. Apalkov, and M. I. Stockman, "Topological resonance and single-optical-cycle valley polarization in gapped graphene," Phys. Rev. B **100**, 115431 (2019).

[38] S. Y. Zhou, G. H. Gweon, A. V. Fedorov, P. N. First, W. A. de Heer, D. H. Lee, F. Guinea, A. H. Castro Neto, and A. Lanzara, "Substrate-induced bandgap opening in epitaxial graphene," Nat. Mater. **6**, 770 (2007).

[39] M. S. Nevius, M. Conrad, F. Wang, A. Celis, M. N. Nair, A. Taleb-Ibrahimi, A. Tejeda, and E. H. Conrad, "Semiconducting graphene from highly ordered substrate interactions," Phys. Rev. Lett. **115**, 136802 (2015).

[40] S Azar Oliaei Motlagh, Fatemeh Nematollahi, Aranyo Mitra, Ahmal Jawad Zafar, Vadym Apalkov, and Mark I Stockman, "Ultrafast optical currents in gapped graphene," Journal of Physics: Condensed Matter **32**, 065305 (2019).

[41] Yu-Ting Wang, Chih-Wei Luo, Atsushi Yabushita, Kaung-Hsiung Wu, Takayoshi Kobayashi, Chang-Hsiao Chen, and Lain-Jong Li, "Ultrafast multi-level logic gates with spin-valley coupled polarization anisotropy in monolayer mos2," Scientific Reports **5**, 8289 (2015).

[42] Zhaogang Nie, Run Long, Linfeng Sun, Chung-Che Huang, Jun Zhang, Qihua Xiong, Daniel W. Hewak, Zexiang Shen, Oleg V. Prezhdo, and Zhi-Heng Loh, "Ultrafast carrier thermalization and cooling dynamics in few-layer mos2," ACS Nano **8**, 10931–10940 (2014).

[43] M. Breusing, S. Kuehn, T. Winzer, E. Malic, F. Milde, N. Severin, J. P. Rabe, C. Ropers, A. Knorr, and T. Elsaesser, "Ultrafast nonequilibrium carrier dynamics in a single graphene layer," Phys. Rev. B **83**, 153410 (2011).

[44] D. Brida, A. Tomadin, C. Manzoni, Y. J. Kim, A. Lombardo, S. Milana, R. R. Nair, K. S. Novoselov, A. C. Ferrari, G. Cerullo, and M. Polini, "Ultrafast collinear scattering and carrier multiplication in graphene," Nat Commun **4**, 1987–1–9 (2013).

[45] I. Gierz, J. C. Petersen, M. Mitrano, C. Cacho, I. C. Turcu, E. Springate, A. Stohr, A. Kohler, U. Starke, and A. Cavalleri, "Snapshots of non-equilibrium Dirac carrier distributions in graphene," Nat. Mater. **12**, 1119–24 (2013).

[46] Andrea Tomadin, Daniele Brida, Giulio Cerullo, Andrea C. Ferrari, and Marco Polini, "Nonequilibrium dynamics of photoexcited electrons in graphene: Collinear scattering, Auger processes, and the impact of screening," Phys. Rev. B **88**, 035430 (2013).

[47] W. V. Houston, "Acceleration of electrons in a crystal lattice," Phys. Rev. **57**, 184–186 (1940).

[48] F. Bloch, "Über die Quantenmechanik der Elektronen in Kristallgittern," Z. Phys. A **52**, 555–600 (1929).

[49] F. Wilczek and A. Zee, "Appearance of gauge structure in simple dynamical systems," Phys. Rev. Lett. **52**, 2111–2114 (1984).

[50] D. Xiao, M.-C. Chang, and Q. Niu, "Berry phase effects on electronic properties," Reviews of Modern Physics **82**, 1959–2007 (2010).

[51] F. Yang and R. B. Liu, "Nonlinear optical response induced by non-Abelian Berry curvature in time-reversal-invariant insulators," Phys. Rev. B **90**, 245205 (2014).

[52] Guilmot Ernotte, T. J. Hammond, and Marco Taucer, "A gauge-invariant formulation of interband and intraband currents in solids," Phys. Rev. B **98**, 235202 (2018).

[53] H. K. Kelardeh, V. Apalkov, and M. I. Stockman, "Graphene in ultrafast and superstrong laser fields," Phys. Rev. B **91**, 045439–1–8 (2015).

[54] F. Nematollahi, S. A. O. Motlagh, V. Apalkov, and M. I. Stockman, "Weyl semimetals in ultrafast laser fields," Phys. Rev. B **99**, 245409–1–9 (2019).

[55] F. Nematollahi, V. Apalkov, and M. I. Stockman, "Phosphorene in ultrafast laser field," Phys. Rev. B **97**, 035407–1–6 (2018).

[56] Christian Heide, Tobias Boolakee, Takuya Higuchi, and Peter Hommelhoff, "Sub-cycle temporal evolution of light-induced electron dynamics in hexagonal 2d materials," Journal of Physics: Photonics **2**, 024004 (2020).